Plasmonic effect and bandgap tailoring of Ag/Ag_2S doped on ZnO nanocomposites for enhanced visible-light photocatalysis

Emmanuel O. Ichipi[a,*], Shepherd M. Tichapondwa[b], Evans M. N. Chirwa[a]

[a] *Water Utilisation and Environmental Engineering Division, Building 2, South campus*

[b] *Department of Chemical Engineering, University of Pretoria, Pretoria 0002, South africa*

Highlights

- ZnO wide bandgap is limited by high e^-/h^+ recombination rate and UV light activation.
- Ag_2S narrowed the bandgap and SPR effect of Ag^+ ion activates the optical properties.
- Forensic investigation identify holes and superoxides as the main degradation drivers.
- Declining stability performance of the composite during five recycle runs.
- •Visible light absorption enhancement by the proposed composite mechanism.

Graphical Abstract

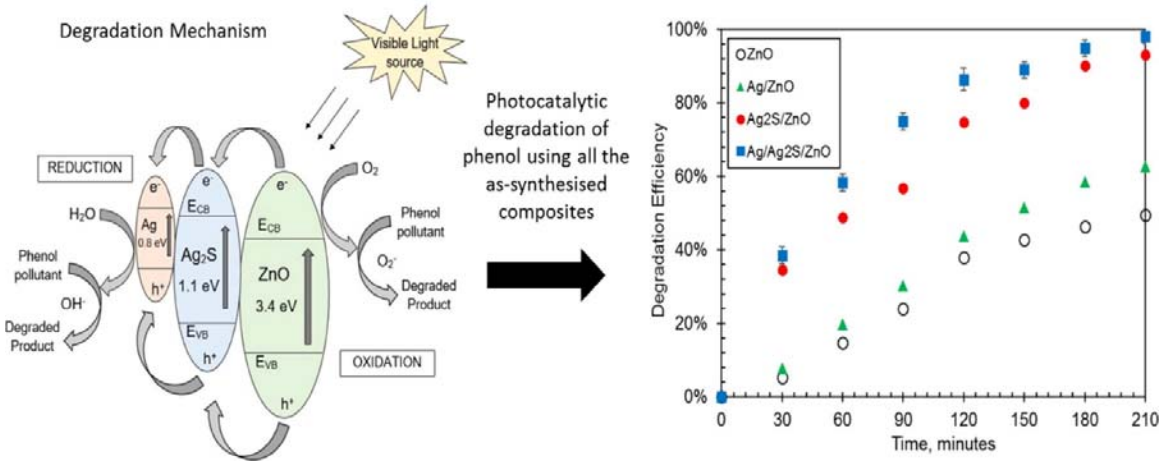

Abstract

Ag/Ag_2S-ZnO nanocomposites were prepared via a simple hydrothermal process followed by a plasmonic Ag^+ reduction through a photo-deposition method. Ag_2S was introduced to narrow the overall composite bandgap and activate the surface plasmon resonance (SPR) effect of the Ag^+ cation present. The physicochemical properties of the as-synthesised catalysts were characterised by X-ray diffraction (XRD), scanning and transmission electron microscopies (SEM and TEM), Brunauer-Emmett-Teller (BET) analysis. Fourier-transform infrared spectroscopy (FTIR), Ultraviolet diffuse reflectance spectroscopy (UV-vis DRS), photoluminescence emission spectra (PL) and X-ray photoelectron spectroscopy (XPS) was conducted to investigate the photo-absorption and emission spectra of the nanocomposites. The degradation efficiency of all the synthesised catalysts (ZnO, Ag_2S, Ag/ZnO and Ag_2S/ZnO) prior to the final product, Ag/Ag_2S/ZnO was tested and compared. Results showed that the ternary Ag/Ag2S/ZnO achieved a 98 % phenol removal compared to 50 %, 11 %, 64 % and 93 % for ZnO, Ag2S, Ag/ZnO and binary Ag2S/ZnO, respectively. The degradation kinetics followed the Langmuir-Hinshelwood model, which typically describes heterogeneous photocatalytic surface reactions. The linear fits had R^2 values higher than 0.97, which confirms the degree of accuracy or statistical fitness to the kinetic model. Degradation scavenger test confirmed the holes (h^+) as the main inhibitor and identified the superoxide $O_2\bullet^-$ radical as the main active specie responsible for the degradation. Total organic carbon analysis using the ternary Ag/Ag_2S-ZnO catalyst only achieved a 74% phenol mineralization after 24 hours of photocatalysis. Recyclability tests showed good phenol removal stability of Ag/Ag_2S-ZnO at 41 % after five recycle runs. Hence, a synergistic degradation mechanism responsible for the efficient photo-degradation performance was proposed.

Keywords: Ag/Ag_2S doping, hydrothermal, Langmuir-Hinshelwood kinetics, photo-deposition, Surface plasmon resonance (SPR).

1. Introduction

Remediation of new classes of organic pollutants is an ever-increasing problem globally due to the recalcitrant nature and the broad array of compounds being released from industry, hospitals, homes and agricultural. Over the years, several methods have been developed and new ones have been proposed to resolve the problem of pollution containing recalcitrant organics. However, most of the currently used treatment strategies are limited by process complexity and operational cost. Researchers have therefore extensively explored the effectiveness of water treatment by advanced oxidation processes (AOPs) due to their great potential to remove a variety of organic recalcitrants in aqueous medium [1]. Semiconductor photocatalysis has proven to be one of the best AOP with great potential to completely remove micropollutants and organic compound from water leaving little or no traces behind [2]. Moreover, photocatalytic and photolytic processes have been shown to completely mineralise organic compounds to CO_2 and H_2O under the right conditions [3]. Commonly used semiconductor photocatalysts such as TiO_2, ZnO, FeO, etc., are limited by their fast electron-hole recombination rate and high consumption of energy in the UV range for efficient performance [4]. TiO_2 is a readily available and non-toxic semiconductor photocatalyst with a wide bandgap energy of 3.2 eV but can only utilize UV light, which constitutes 4 - 5 % of the entire solar energy [5-7]. ZnO semiconductor photocatalysts has been extensively investigated as a substitute to TiO_2 owing to their similar properties [8]. Their large surface

area and high photosensitivity is an added advantage however, it is still limited to the UV range [9].

Strategies have been proposed to overcome these limitations through the development of a new generation semiconductor photocatalysts with the potential of harnessing solar visible light and inhibiting recombination rate [10]. The development of novel visible-light active composites using various approaches including the use of metal organic frameworks (MOFs), metal and/or non-metal doping, surface-dye sensitization, plasmonic deposition, has been pivotal in improving degradation performance [6]. Oxidised states of base and earth metals such as Fe, Mn, Co, Cu, Ga, Ce, Ni promote surface charge separation/transfer and also act as traps to capture photo-generated e^-/h^+ pairs. However, since some of these metals are not thermodynamically stable, researchers have proposed the use of non-metal ions like C, N which can be used in combination with oxidized base metals [11].

Recent studies have reported the use of MOFs photocatalysts, a green technology in the treatment of wastewaters [12, 13, 14]. They are mesoporous metal based crystalline adsorbents, which are characterised by wide bandgap energy, high surface reaction, selectivity and stability. However, they are limited by poor recyclability due to high sludge generation [15]. Like several powdered semiconductors, MOFs can be modified with precious metals and incorporated into film membranes to inhibit electron-hole recombination, increase photosensitivity and improve recyclability [16]. Ag, Pd metals grown into a crystalline MIL-125-NH_2 disc within cellulose acetate catalysts, exhibited high visible light photo-reduction of 2-nitrophenol solutions (80.6 - 93.5 %) and good showed stability (54.4 - 62.0 %) after five recycling runs [17].

A review on the versatility of doping different transition metals including other metal oxides on ZnO nanoparticles revealed the possibility bandgap tailoring and optical/magnetic property enhancement [18]. The doping effects of 3 wt% Cu on ZnO thin films resulted in narrowing of bandgap energy from 3.03 to 2.7 eV as well as a red-shift of absorption band edge to about 450 nm to the visible light region [19]. Fe and Co optimally co-doped on ZnO mesocrsytals resulted in higher photocatalytic activity by 145 % owing to the multivalent ferromagnetic state of the Fe and Co ions [20]. Some noble metals like Ag and Au can exhibit strong surface plasmonic resonance (SPR), which can be mechanised by photo-deposition to enhance its unique optical properties and visible light absorption [21, 22]. Upon illumination, the electromagnetic rays cause a collective oscillation of electrons at the conduction band of the photocatalyst and amplifies its optics for visible light absorption [23]. Using the glancing angle deposition method, the SPR emission of ZnO was enhance with plasmonic Ag nanorods from 384 nm (3.23 eV) to 396 nm (3.13 eV) [24]. The SPR enhancement of ZnO was found to be dependent on its surface morphology and Ag deposition interlayers which match the surface plasmons to the emission band energies [25]. The SPR of the Au nanoparticles capped on ZnO nanorods showed a remarkable enhancement of the UV emission intensities and complete suppression of a defect related emission as observed on a time-resolved photoluminescence [26]. The bandgap energy of crystalline $(GaN)_{1-x}(ZnO)_x$ nanowires was tailored from 3.08 to 2.77 eV using Au-assisted VLS mechanism for solar light induced photoelectrochemical splitting of water [27].

In this study, Ag_2S nanoparticles are incorporated in ZnO nanospheres via a hydrothermal synthesis method in order to improve its photo-absorption and inhibit electron-hole pair recombination rate. Furthermore, as-synthesised binary Ag_2S-ZnO is photo-deposited to

activate the SPR effect of the Ag constituent photocatalyst into ternary Ag/Ag_2S-ZnO. The prepared nanocomposites are investigated in the degradation of phenol, a common toxic organic recalcitrant present in industrial wastewaters under visible-light irradiation. It is expected that the plasmonic effect and metal doping of ZnO may significantly improve the visible-light absorption, separation of charges and overall degradation performance of the catalyst. A possible mechanism to account for the improved photocatalytic activity based on the combined effort of metal doping and SPR were explored in detail.

2. Experimental

2.1. Synthesis of photocatalyst materials

The nanocomposites were prepared through a simple hydrothermal method followed by photo-deposition to activate the plasmonic effect of the Ag particles. ZnO was prepared by dissolving 4.46 g of Zn $(CH_3COO)_2.2H_2O$ in 100 mL of 0.2 M NaOH and distilled water. The mixture was autoclaved at 120 °C for 2 h to form a white precipitate. The precipitate was washed 3 times each with distilled water and ethanol, every time, it was centrifuged, and the supernatant discarded before drying in an oven. In order to eliminate all the volatile substances present in the catalyst, ZnO was calcined in a furnace at 900 °C for 3 h and then ground to powder. Ag-ZnO was synthesised by suspending 3 g of the as-prepared ZnO and 0.24 g of $AgNO_3$ in 150 mL of 60/40 % methanol/distilled water mixture. The mixture was placed in an ultrasonicator for 40 minutes to rigorously shake the particle mixture; it was labelled as the composite precursor. To activate the plasmonic effect of the Ag constituent, one-quarter portion of precursor solution was stirred under visible light for 2 hours and labelled as sample A.

0.18 g of Na_2S was added with constant stirring, to the remaining three-quarter portion of the composite precursor and divided into halves. For the binary Ag_2S-ZnO composite, one half of the solution was magnetically stirred in the dark for 8 h to prevent a SPR photo-reduction of the Ag constituent and labelled as sample B. Ternary Ag/Ag_2S-ZnO composite was prepared by stirring the other half under visible light for 2 hours. A color change from brown to purple indicated that the Ag^+ cation has been photo-reduced to Ag^0 as previously reported in literature [28].

The precipitates formed in sample A, B, and C were collected by centrifugation at 9000 rpm and dried overnight at 70 °C in an oven. All the samples were ground to fine powder using a mortar and pestle before they were used. A pictorial summary of the synthesis procedure is illustrated in Fig 1.

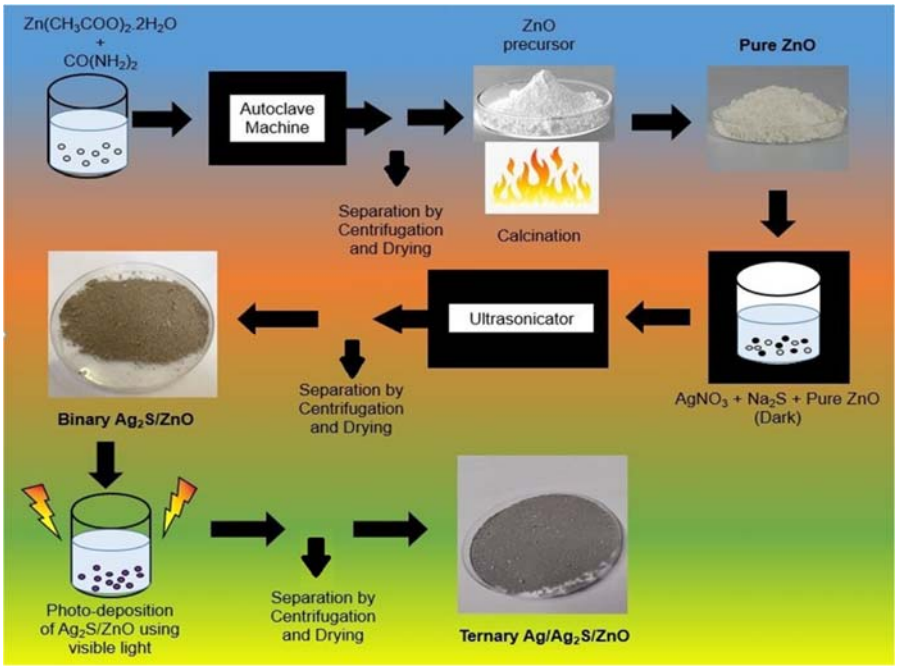

Fig. 1: Pictorial illustration of Ag/Ag_2S-ZnO composites synthesis

2.2. Material Characterization

X-ray diffraction (XRD) spectra of all the catalysts were obtained using a PANalytical X'Pert Pro powder diffractometer in θ–θ configuration with an X'Celerator detector, a variable divergence and fixed receiving slits with Fe filtered Co-Kα radiation (ʎ =1.789Å). The crystallinity of the samples was determined by selecting the best-matching patterns from an X'pert Highscore plus software database. Scanning electron microscope (SEM) images were captured using a Zeiss Ultra PLUS FEG SEM installed with an Oxford instruments detector and AZtec 3.0 software SP1. Prior to the analysis the samples powders were dispersed on a carbon tape, stripped firmly to and aluminium plate and coated with carbon in a SEM auto-coating unit E2500. High-resolution transmission electron microscopy (HRTEM) imaging was captured using a JOEL JEM 2100F, 200 kV analytical electron microscope. The sample powders were meshed to a Formvar film and layered with a light carbon for stability upon exposure to the electromagnetic beam. Brunuaer-Emmett-Teller (BET) surface areas of the materials were determined using a micrometrics TriStar II 3020 Version 3.02 BET system. The sample powders were outgassed overnight to remove all the absorbed gases and moisture content using pure nitrogen flow at 100°C. The N_2 adsorption-desorption isotherms were obtained at a boiling temperature of 77.350K liquid nitrogen at 5secs equilibration interval. A PerkinElmer 100 Fourier-transform infrared (FTIR) spectrometer, MIRacle Zn/Se instrument was used to identify the chemical and functional groups present in the samples. The samples spectra scan for the samples were detected within a wavelength range from 4000 to 400 cm^{-1}. Ultraviolet-visible diffuse reflectance spectra (UV-vis DRS) to determine the absorption and bandgap energy of the materials were obtained from a Hitachi U-3900 double-beam single-monochromatic system with a UV-solutions software program. The sample powders were

suspended in distilled water to a known concentration and placed in a clean cuvette for analysis. The absorption spectra were detected at a scan speed of 600 $nmmin^{-1}$ and wavelength range from 1100 to 350 nm. Photoluminescence spectra to determine the emission potential of the materials was conducted using a FlouroMax-4 spectrofluorometer series, HORIBA scientific, installed with a FluorEssenceTM software for data analysis. The monochromators are Czerny-Turner design with plane gratings for optimized focus at all wavelengths and minimum stray light. The base detector is a Photomultiplier R928P with spectral coverage ranging from 200 – 870 nm. X-ray photoelectron spectroscopy (XPS) analysis to determine the elemental compositions and electrochemical states of constituents at the surface was done using a Thermo Fisher scientific ESCALAB 250Xi with a monochromatic Al Kα X-ray source (1486.7 eV) operated at 300 W. To determine the thermal stability and volatility of the samples TGA5500 from TA instruments was used at a heating rate of 10 $°Cmin^{-1}$ ranging from 25 - 1000°C under inert nitrogen gas

2.3. Experimental

2.3.1. Reactor setup

The experimental setup consisted of a wooden box fitted with three Philips 18 W fluorescent day light lamps to simulate visible light irradiation as shown in Fig 2. The luminous flux of the lamp according to the product specification is 1200 lm each. The box was inner lined with aluminium foil paper to support even distribution and reflection of the light. Three magnetic stirrers were placed inside the box about 10 cm from the lamps to continuously stir three batches of the slurry solution. The light intensity was calculated using the wattage and

distance of the reactor from the lamp and found to be 142.857 W/m^2. The temperature of the reaction was monitored with a thermometer placed in the box and it was found to be 30 °C (±5). A triplicate of runs was performed for the purpose of averaging results.

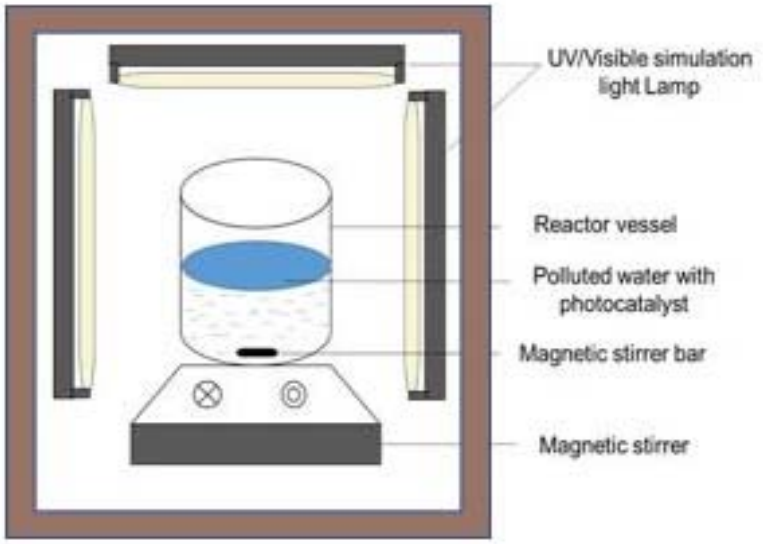

Fig. 2. Schematic batch reactor set-up

2.3.2. Degradation experiments

All the tests were conducted by dispersing 0.4 g/L catalyst in a 100 mL synthetic phenol in water of 10 mg/L concentration. The solutions are magnetically stirred at 190 rpm under visible light irradiation for 3.5 hours. At every 30 minutes interval, 2 mL samples were withdrawn from the reaction and centrifuged. The supernatant is drawn with a syringe and passed through a 0.45 µm Millipore filter into HPLC sample vial bottles for analysis. The photolysis (with light only) and adsorption (with catalyst in the dark) tests were conducted in the same procedure and conditions. For the photocatalysis tests, the solution was first stirred in the dark for 30 minutes to reach adsorption-desorption equilibrium before the illumination for 3.5 hours. Optimization studies to determine the optimum degradation conditions was

carried out while varying factors like pH, initial concentration, and catalyst dosage. The initial pH of the solution was adjusted with either HCl or NaOH and measured using a Celsius scientific PL-700AL pH meter with glass electrode. The percentage of photo-degradation achieved for each experiment is determined following the expression;

$$\text{Percentage Degradation} = \frac{(C_0 - C_t)}{(C_0)} \times 100 \quad (1)$$

where C_0 is the initial phenol concentration before and C_t the final phenol concentration after irradiation time, t.

The progressive degradation of phenol was monitored using a Waters 2695 HPLC with a 2996 Photodiode Array detector and Empower software. Phenol was detected in a PAH C18 (4.6 x 250 mm, 5 µm) column at an injection volume of 10 µL, a flow rate of 1.0 $mLmin^{-1}$ and wavelength of 283 nm. The mobile phase was a mixture of 1 % acetic acid in water and acetonitrile at 50 % elution each. Degradation intermediates were identified using a PerkinElmer GC-MS – Clarus 600 T MS system compactible with a Clarus 600 GC with Elite 5MS GC capillary column with dimensions, 250 µm x 30 m. A Shimadzu TOC-V analyzer instrument was used to quantitatively analyze the extent of phenol mineralization before and after photocatalysis.

In order to determine the dominant reacting species, various scavenging tests were performed. This was conducted by adding 5×10^{-3} mol/dm^3 of isopropyl alcohol (IPA for the OH• radicals), p-benzoquinone (pBZQ for the $O2•^-$ radicals), triethanolamine (TEA, for the h^+ V_B) and Cupper (II) nitrate (C2N for the e^- C_B). Recyclability tests to investigate the stability of the ternary Ag/Ag_2S-ZnO catalyst were also conducted. After each run, a sample is withdrawn and set aside for analysis while the rest of the solution is centrifuged at 9000 rpm for 10

minutes followed by decantation. The catalyst particles are dried and re-dispersed into a fresh phenol solution for another run.

3. Results and discussion

3.1. Material characterization

The crystallinity and structural phase of the synthesised composites were examined by XRD and the spectra are shown in Fig 3. ZnO naturally exist as a hexagonal wurtzite structure with the lattice constants a = b = 0.3249 nm, c = 0.52042 nm and specific mass density of 5.68 gcm^{-3} at ambient conditions [29]. The patterns and values of the as-prepared ZnO composites matches precisely with standard data (JCPSD card #36-1451) indicating that the desired powders were purely synthesised. The peaks were intense and sharper at (100), (002), (101), (102), (110), (103) and (112) planes which shows the high purity of hexagonal wurtzite crystals of the ZnO catalyst [29]. All the XRD patterns of the catalysts reflect the existence of ZnO peaks; however, a new peak was noticed at 45° in the ternary Ag/Ag_2S-ZnO spectra signifying the presence of Ag [30]. The typical size of silver sulphide (2 – 5 nm) is much smaller than the minimum penetration depth of the XRD beam (approx. 2 – 3 μm) [31]. Furthermore, the low crystallinity of Ag_2S and high difference between the metallic properties of Zn and Ag may be a reason for little/no detection.

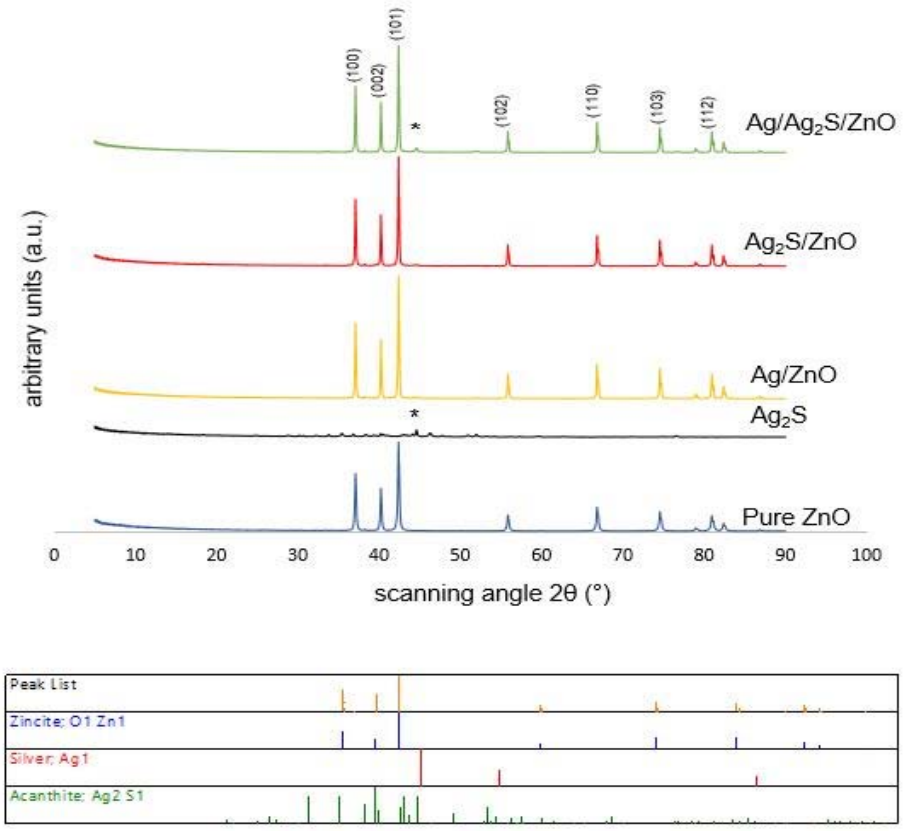

Fig. 3. XRD Spectra for ZnO, Ag/ZnO, Ag_2S-ZnO and Ag/Ag_2S-ZnO composites.

The morphology of the composites was analysed by SEM and the captured images are presented in Fig 4a - d. ZnO resembles a flower-like structure with flakes of approximately 50 nm thick while Ag/ZnO showed clusters of spherical nanoparticles. The SEM images for Ag_2S-ZnO and Ag/Ag_2S-ZnO revealed a mixed agglomerate with angular/cube like structures with wide particle size distribution about 100 nm and reduced to approximately 50 nm upon photo-deposition. The change in morphology can be attributed to effect of the Ag_2S doping and plasmonic of Ag as literature reported [32]. The SPR effect of Ag causes clusters of grains deposits to form on the surface composite [33].

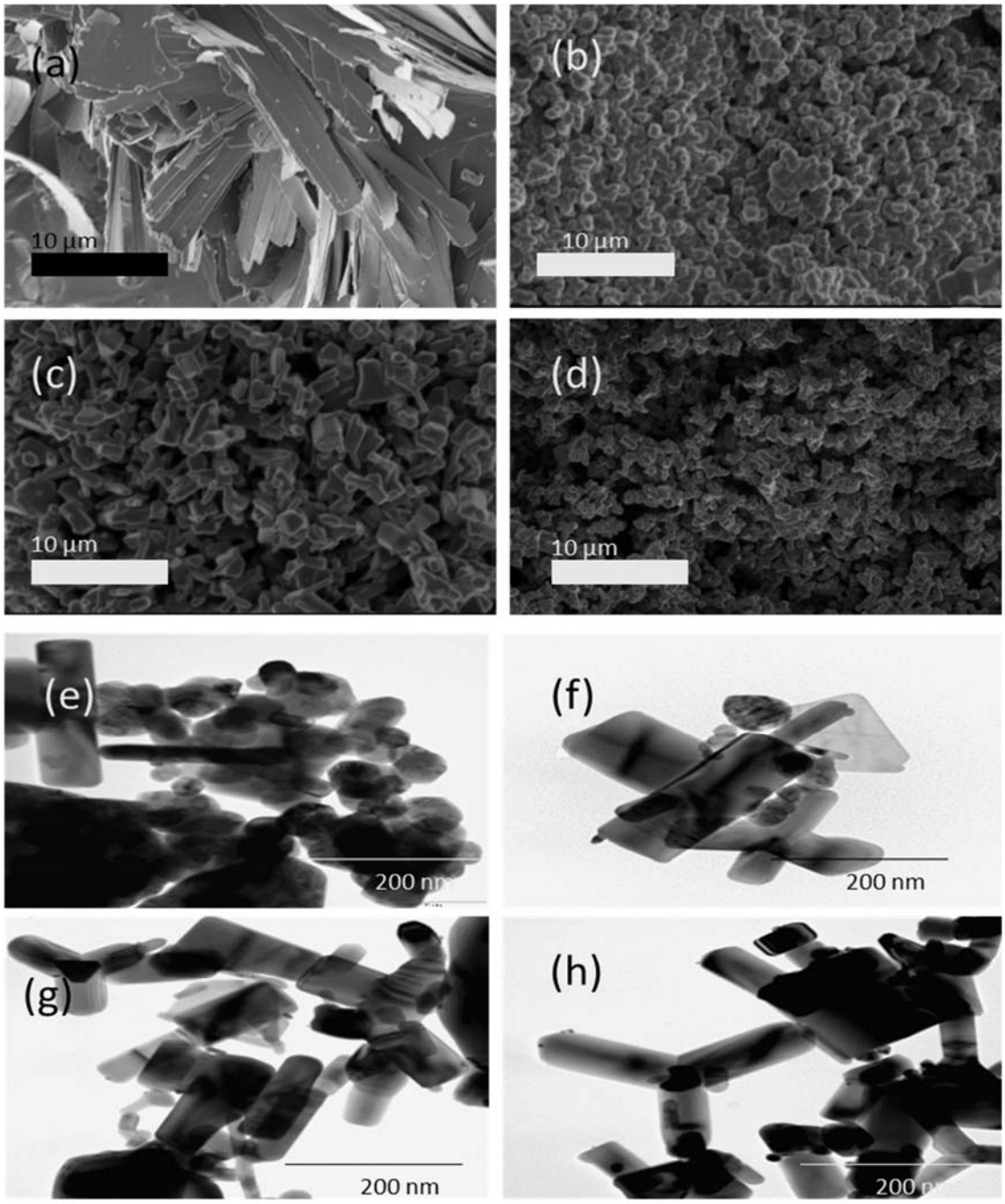

Fig. 4. SEM images for synthesised (a) ZnO; (b) Ag/ZnO; (c) Ag_2S-ZnO; (d) Ag/Ag_2S-ZnO composites; High-resolution TEM images for synthesised (e) ZnO; (d) Ag/ZnO; (f) Ag_2S-ZnO and (g) Ag/Ag_2S-ZnO composites.

High-resolution TEM images of the composites are revealed in Fig 4e - h. Rod-like structure decorated with spherical and hexagonal structures stacked layer by layer was detected for ZnO ranging from 10 – 30 nm. The metallic Ag clusters formed on the exterior of the silver modified composites indicated and interlayer d-spacing of 0.25 nm corresponding to the (111) plane of Ag in JCPDS card #87-0597 [32]. The images showed good dispersion of the Ag_2S particles even though some layers were overlapping. A trigonal planar geometry was identified in TEM images of Ag_2S-ZnO and Ag/Ag_2S-ZnO, the darker portion represents the electron-dense region.

Surface area width plays an important role in photocatalytic degradation since larger surface areas will have more active sites for reaction. The specific surface area and micropore size distribution of all composites was calculated by N_2 adsorption isotherms and summarized in Table 1. An insignificant reduction in the surface area of ZnO to Ag_2S-ZnO from 4.95 to 4.62 m^2g^{-1} was attributed to the doping effect of a low surface area Ag_2S material [34]. This resulted to the collapse of pores and reduction of particles sizes; however, the surface area was regained upon photo-reduction of the Ag particles due to the effect of SPR of the photo-excited electrons at the surface [30]. The external surface area was observed to have increased consistently with a decrease in micropore area for all the composites. The BET isotherm for ternary Ag/Ag_2S-ZnO in Fig. 5a is identified as a type IV according to IUPAC with an H3 hysteresis loop indicating that microporous material was synthesised [35]. The step-down in adsorption-desorption isotherm curves is as a result of the spontaneous evaporation of metastable pore liquid known as “Cavitation” [36].

Table 1: BET surface area charateristics

Catalyst	BET surface Area (m^2g^{-1})	Relative surface area (%)	Ext. surface area (m^2g^{-1})	Micropore area (m^2g^{-1})
ZnO	4.948	100	2.754	2.194
Ag/ZnO	4.689	95	2.621	2.069
Ag_2S/ZnO	4.622	93	3.061	1.561
Ag/Ag_2S/ZnO	4.954	100	3.226	1.728

The FTIR data of the composites were collected in the range of 500 to 4000 cm^{-1} and shown in Fig 5b. The band of peaks formed in the ZnO spectra between 1850 and 2500 cm^{-1} were apportioned to the C-H bond stretching by vibration of the alkane groups while the broad band between 3527 and 3960 cm^{-1} was due to the vibration stretching of the OH group. The reoccurring peaks observed at 760 and 1048 cm^{-1} in all the composites were ascribed to the asymmetrical and symmetrical stretching of the zinc carboxylate and C=O group of esters, respectively. The optical photo-absorption bands observed at 608 and 726 cm^{-1} is corresponding to the E2 mode of hexagonal ZnO (Raman active) and 1330 cm^{-1} may be associated with oxygen deficiency and/or oxygen vacancy (VO) defect complex in the ternary composites [37].

The optical and photo-absorption properties of the synthesized catalysts were examined by UV-vis DRS and the results are revealed in Fig 5c. ZnO showed absorption in the UV range at 340 nm, but a red-shift towards the visible light region is observed about 400, 420 and 435 nm for Ag/ZnO, Ag_2S-ZnO and Ag/Ag_2S-ZnO respectively. The red-light shifting of ZnO can be ascribed to the improvement of shallow bandgap levels caused by external atoms in the lattice of ZnO and SPR effect of the Ag particles [38]. The shift in light absorption peak and

wavelength range confirms that the optical bandgap has be reduced and this can be estimated with as;

$$E_g\ (eV) = (hc/\lambda) \quad (2a)$$

Where E_g is the optical bandgap energy, h is Planck's constant, c is the speed of light and λ is the maximum absorption wavelength. From the absorption spectrum data obtained in Fig 5c, the bandgap energy of each composite was estimated using Tauc plots of absorbance, as obtained from the Kubelka-Munk expression;

$$a = \frac{A}{(hc)} (hc - E_g)^{1/n} \quad (2b)$$

$$(ahc)^2 = A\ (hc - E_g)n \quad (2c)$$

From literature, the direct band transition known for semiconductors is, n = ½ and the photon energy, hc = 1240 nm^{-1} [39, 40]. The optical band gap for each composite was calculated by extrapolating a linear intercept with the hc axis as seen in Fig 5d. The tailored optical bandgap energy of ZnO, Ag/ZnO, Ag_2S-ZnO and Ag/Ag_2S-ZnO were estimated to be 3.2, 2.72, 2.5, and 2.4 eV respectively, indicating that, the bandgap energy has been narrowed by 0.8 eV.

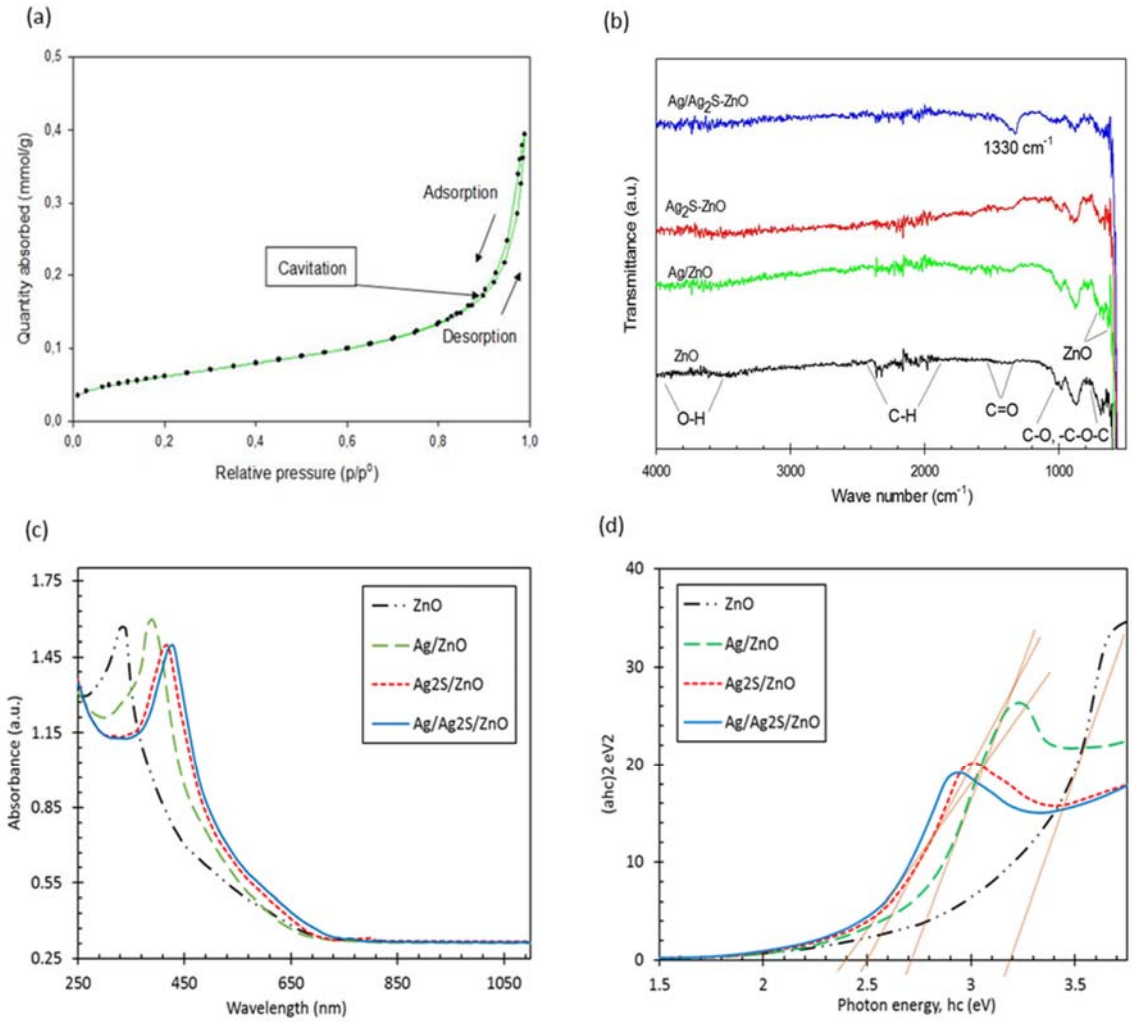

Fig. 5. (a) N_2 adsorption-desorption isotherm for Ag/Ag_2S-ZnO; (b) FTIR spectra of all as-prepared catalyst composites; (c) UV-vis absorption spectra and (d) bandgap estimation by Tauc plots of all the composites.

The emission potential and movement of electrons in the catalysts were investigated at an excitation wavelength of 325 nm, corresponding to ZnO bandgap energy of ~ 3.4 eV under room temperature [41]. In Fig 6a, the PL spectra shows a consistent violet UV emission band peak at around 393 nm and another band around 486 nm which increased in intensity for the modified ZnO catalysts. This can be attributed to several intrinsic defects such as oxygen –

vacancies, interstitials and antisites, a further confirmation of its red-shift to visible light region. The band edge emission at 393 nm is commonly ascribed to the recombination of exciton levels [42]. Ag_2S-ZnO and Ag/Ag_2S-ZnO composites is observed to have lost intensity in the UV region and subsequent gain in the visible light region suggests that, the recombination of photo-generated electron-hole pair has been significantly suppressed [43].

The surface elemental composition and electrochemical states of the composites were investigated using XPS and the results are presented in Fig 6b - f. The survey scan of Ag/Ag_2S-ZnO revealed the presence of Zn, O, Ag, C, Cl and S in Fig 5b. The Ag3d spectrum identified two major peaks consistent at binding energy of 367.1 eV and 373.03 eV, which corresponds to the reported values for $Ag3d_{5/2}$, and $Ag3d_{3/2}$ signals of Ag^+ in Ag_2S compound [44, 45]. The smaller peaks at 367.3 eV and 347.4 eV are ascribed to the photo-reduced Ag^0 form of the Ag compound. It was noticed that the intensity of the Ag peaks increased upon photo-reduction in agreement with the color change that was observed during the composite synthesis. The Zn major peak is identified at a binding energy of 1021.4 eV and another characteristic peak at 1045.3 eV conforming to $Zn2p_{3/2}$ and $Zn2p_{1/2}$ which implies that the zinc element is in a Zn^{2+} chemical state [31]. The O1s and C1s spectrum of Ag/Ag_2S-ZnO in Fig 6e and f respectively, showed fitted peaks of C=O, C-O, C-C, and O-C=O bonds identified as water and radicals. Ag^0 photo-reduction improves photocatalytic degradation efficiency following the adopted expression [46];

$$Ag^0 + e^- \rightarrow Ag^- \quad (3a)$$

$$Ag^- + O_2 \rightarrow O_2^{\bullet -} + Ag^0 \quad (3b)$$

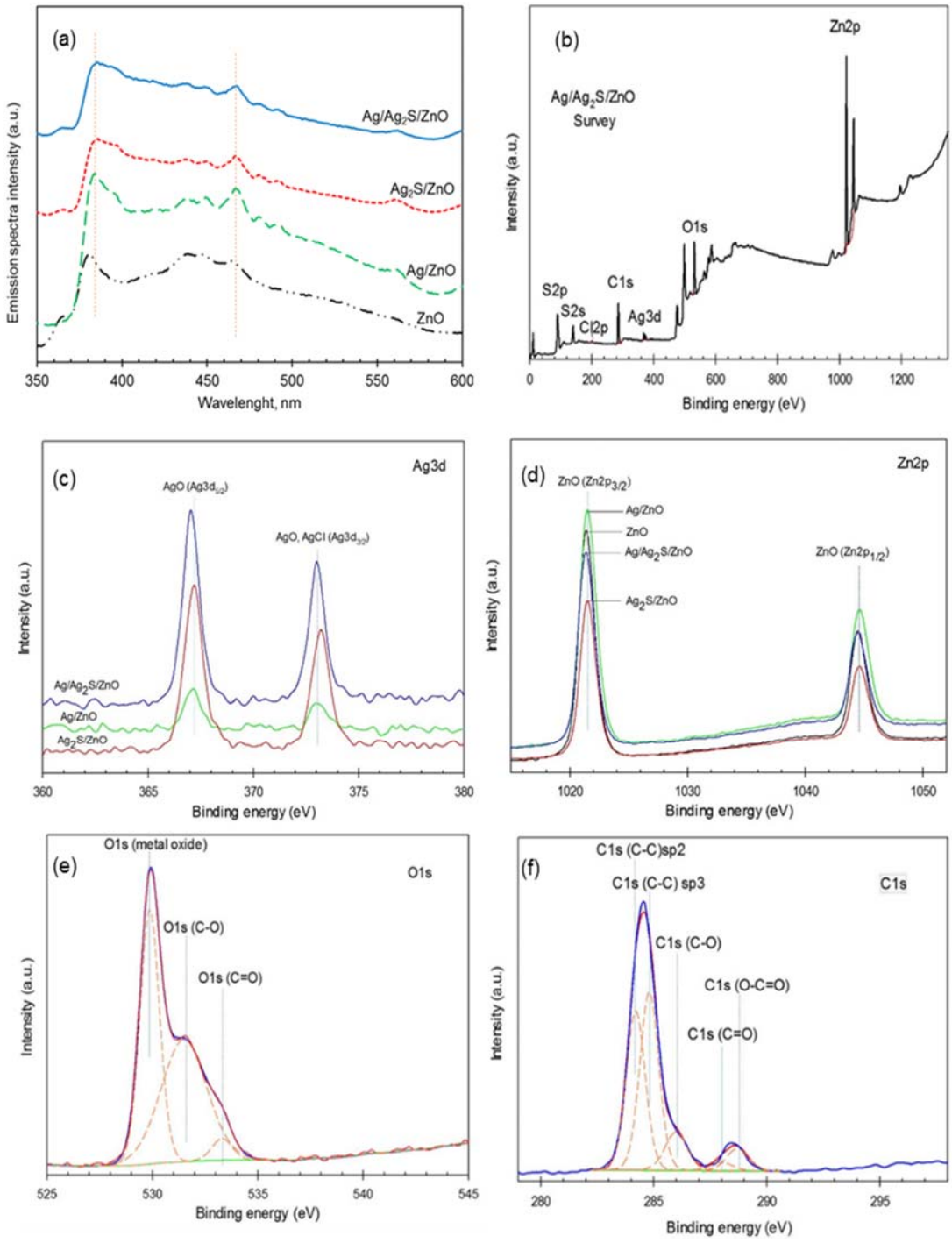

Fig. 6. (a) Photoluminescence spectra of all synthesised catalyst adjusted into arbitrary units; (b) Survey spectra for ternary Ag/Ag_2S-ZnO; (c) Ag3d XPS spectra for Ag/ZnO, Ag_2S-ZnO and Ag/Ag_2S-ZnO composites; (d) Zn2P, (e) O1s, and (f) C1s XPS spectra for all the as-prepared composites.

3.2. Photolysis, adsorption and photocatalytic degradation activity

Preliminary degradation investigations were carried out by conducting control experiments. Here, visible light alone (photolysis) and the catalysts alone in the absence of light (adsorption) were exposed to the phenol solution of the pollutant and adsorption capacity of the catalyst composites, and the results are presented in Fig 7a. The Photolysis test recorded negligible phenol removal (5 %) while adsorption using Ag/Ag_2S-ZnO resulted in 14 % phenol removal. removal of phenol with light irradiation only. This was attributed to the adsorption of the phenol molecules on to the active sites present on the surface of the catalyst. However, the same Ag/Ag_2S-ZnO composite had a near complete degradation of 98 % under visible light irradiation. The increase in performance was assumed to be attributed to the photo-generated degradation species that enhances the rate of the reaction. These tests, therefore, confirm that both light and catalyst must combine under the right conditions for an effective photocatalytic degradation.

3.2.1. Individual catalyst composite

As indicated in Fig 7b, each of the synthesised catalyst has its own unique bandgap energy, which can be activated by different types of light based on the spectrum wavelength. The efficiency of the each of the catalyst composites was compared in the degradation of phenol. Fig 7c, shows that ZnO had the least activity (50 %) compared to the binary Ag/ZnO and Ag_2S-ZnO composites that achieved 64 % and 93 % phenol removal efficiency, respectively. As expected the ternary catalyst Ag/Ag_2S-ZnO recorded the highest phenol degradation of 98 %. The improvements in degradation efficiency were ascribed to the effect of bandgap narrowing

by metallic doping and SPR dipolar effect of Ag^{+} ions of Ag/Ag_2S on the overall composite. However, excess Ag photo-deposition on the composite surface may lead to light hindering and low degradation activity [22]. In comparison, investigations revealed an improved performance in a visible-light driven photoreduction of 2-nitrophenol using Ag and Pd doped in MIL-125-NH_2@CA matrix film. This attributed to overall bandgap reduction of the composite film due to the doping effect of Pd and Ag metals [17]. Other photocatalytic investigations using the ZnO, Ag_2S and Ag, modified with other semiconductor materials as catalyst are reviewed in Table 2.

Table 2: Literature review of Ag, Ag_2S, and ZnO constituents in photocatalysis

Catalyst composite	**UV-Vis wavelength range**	**Pollutant/Dye**	**Degradation**	**Reference**
ZnO/GO	430 nm	Vanillic acid	35 %	[47]
ZnO/Ag_2S@rGO	>375 nm	Acetaminophen	47 %	[48]
ZnO/Ag_2S	700 nm	Methylene blue	90.5 %	[49]
ZnO/Ag	446 nm	Methylene blue	95 %	[50]
Ag_2S	-	SERS detection	78 %	[51]
$GO/Ag/Ag_2S$-TiO_2	584 nm	Crystal violet	80.01 %	[52]
Ag/Ag_2S/rGO	-	Ciprofloxacin	87.6 %	[53]
$Ag/Ag_2S/Bi_2MoO_6$	465 nm	Levofloxacin	87.3 %	[54]
Ag/Ag_2S-ZnO	435 nm	Phenol	98 %	Current work

3.2.2. Effect of catalyst dosage

The amount of catalyst loading is one of the major parameters that affects the efficiency of degradation. This investigation was carried out by varying the amount of the ternary Ag/Ag_2S-ZnO catalyst from 0 to 1 g/L at a 10 mg/L of phenol in water. The results in Fig 7d revealed good photocatalytic activity with 0.4 g/L being the optimum degradation at 98 % degradation. However, a gradual decrease in performance was observed as the catalyst dose was increased to 1 g/L. The decline in reaction rate can be attributed to high turbidity of the suspension and agglomeration of catalyst particles in the reactor. As a result, there is blockage of active sites on the catalyst surface as well as restriction of light penetration for catalyst activation. Likewise, a smaller dosage of the catalyst 0.2 g/L had a lower degradation efficiency at 75 % due to an insufficient number of active sites, less production of free radicals and increased light scattering [55]. Catalyst loading of 0.6, 0.8 and 1 g/L achieved 96, 91 and 83 % degradation respectively.

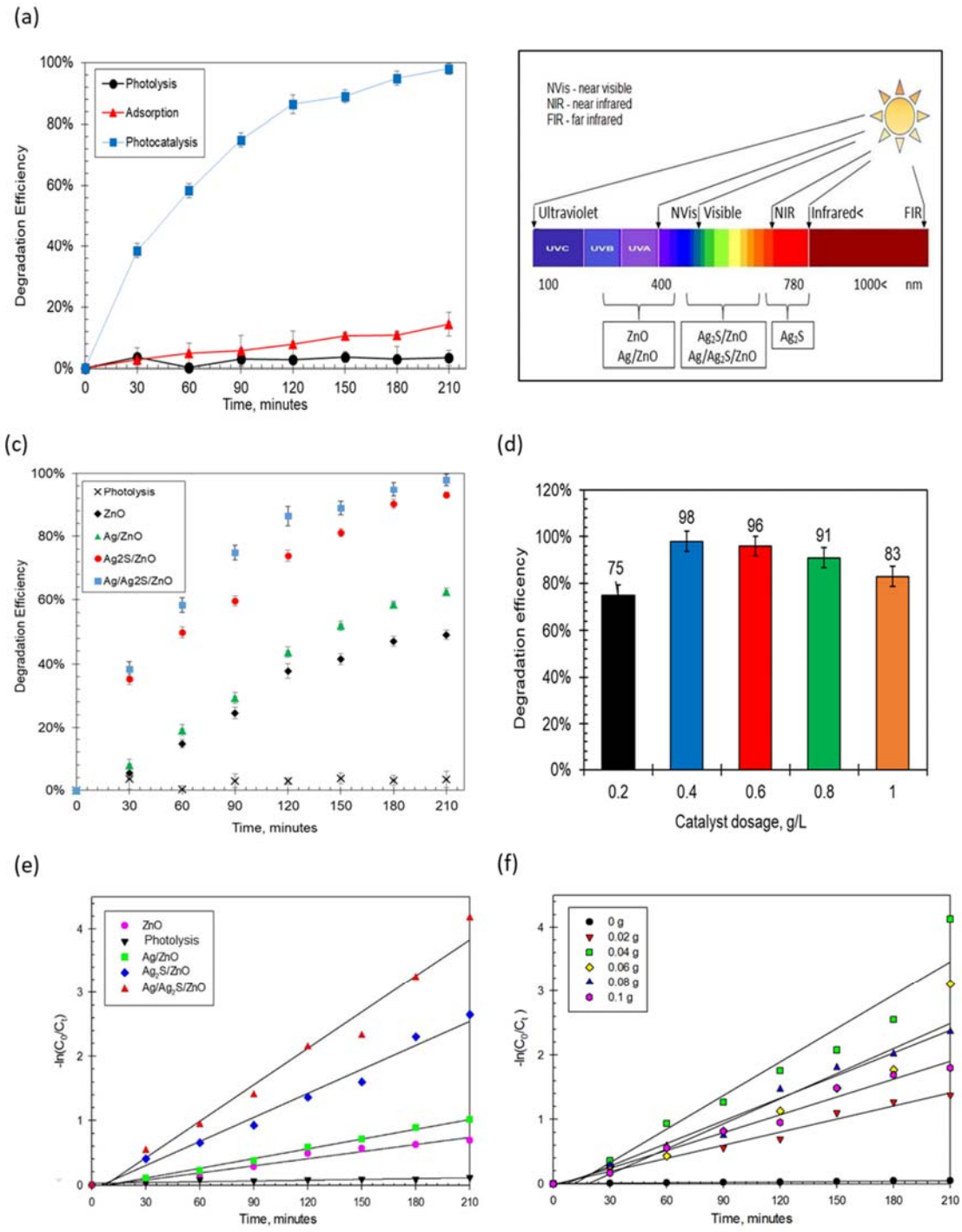

Fig. 7. (a) Photolysis, adsorption and photocatalysis of Ag/Ag_2S-ZnO; (b) Solar spectrum, wavelength and catalyst activation; Photocatalytic degradation (c) performance of composites and (d) effect of Ag/Ag_2S-ZnO catalyst dosage; Linearity kinetics of (e) all the synthesised composites and (e) varying dosage of Ag/Ag_2S-ZnO catalyst.

The results from using the various synthesised composites and the varying catalyst dosages were found to follow the Langmuir-Hinshelwood degradation kinetics model for heterogeneous photocatalytic surface reactions [56], expressed in equation 4a;

$$r = -\frac{dC}{dt} = \frac{k_{max}KC_{phenol}}{1+KC_{phenol}} \quad (4a)$$

where k_{max} (min^{-1}) is the reaction rate constant at maximum experimental conditions. *K* is the Langmuir-Hinshelwood adsorption coefficient and C_{phenol} (mg/L) is the phenol concentration with respect to time, t, during degradation. Equation 4a can be simplified by integration into a pseudo-first-order equation as;

$$k_1 = -\left(\frac{ln\left(\frac{C_t}{C_0}\right)}{t}\right) \quad (lim: C_t = C_0 = C_{phenol} \text{ at } t = 0 = t; \text{ given } k_1 = k_{max}K) \quad (4b)$$

The degradation kinetic model was selected since it can be applied for various photocatalytic systems irrespective of the difference in concentrations and adsorption potential [57]. The rate constants were calculated using Eq. 4b and the comparison of degradation linearity value is fitted in Fig 7e and f. The high degradation rate constant of the ternary Ag/Ag_2S-ZnO (K_1-value = 0.01987 min^{-1}) composite corresponds with it being the highest efficient degradation performance. Likewise, as the catalyst loading is increased from 0 to 0.1 g/L the K_1-values increased and was optimum at 0.04 g. A steady decline above 0.04 g loading was noticed, which is due to particle agglomeration and turbidity in the reactor leading to the blocking of active sites and light penetration.

Chi-square test, (x^2_c), was calculated for the pseudo first order kinetic to check the best fitting data and test the uniform distribution of a “no hypothesis” or “alternative hypothesis” fit. It is expressed as:

$$x_c^2 = \frac{\sum(Observed - Expected)^2}{Expected} \quad (5)$$

This was done using experimentally observed data and an expected complete degradation at a 5 % significance level. For each kinetic study, the degree of freedom, ($df = n - 1$) was calculated based on the number of categories (n) and the area to the right of the critical value, (C_V), was obtained from the chi-square distribution table.

The parameters for the reaction kinetics which includes the rate constants of reaction, chi-square test and regression coefficient (R^2) are shown in Table 3 and 4.

Table 3: Parameters for the reaction kinetic modelling based on catalyst dosage

Catalyst dosage Ag/Ag_2S-ZnO (g/L)	**K_1 x 10^{-3} (min^{-1})**	**Observed Data % Degradation**	**x_c^2 $C_V = 11.071$**	**R^2**
0.2	6.54	75	6.25	0.98
0.4	19.66	98	0.04	0.93
0.6	14.79	96	0.16	0.90
0.8	11.24	91	0.81	0.98
1	8.57	83	2.89	0.98

The lower x^2_c values and higher R^2 values of both kinetic studies confirm the degree of accuracy or statistical fitness of the degradation efficiency to the applied pseudo first order kinetic model [16]. From Table 3, all the calculated chi-square lies in the “do not reject” region which confirms a “no hypothesis” that the experimental data was observed with relatively equal frequencies. Hence the variation in results obtained is not significant to accept an “alternative hypothesis”.

Table 4: Table 2: Parameters for the reaction kinetic modelling based on individual catalysts

Individual catalyst (0.4 g/L, 10 ppm)	K_1 x 10^{-3} (min^{-1})	Observed Data % Degradation	x_c^2 $C_V = 9.488$	R^2
Photolysis	0.23	5	90.25	0.98
ZnO	3.29	50	25	0.97
Ag/ZnO	4.83	64	12.96	0.99
Ag_2S-ZnO	12.63	93	0.49	0.98
Ag/Ag_2S-ZnO	19.87	98	0.04	0.98

In contrast, the calculated chi-square values for photolysis, ZnO and Ag/ZnO lies to the right area of the critical value and rejects the "no hypothesis" as seen in Table 4. However, the binary and targeted ternary catalysts area, lies deep to the left of the critical value and fully satisfy the fitting analysis.

3.2.3. Effect of initial phenol concentration

The influence of initial phenol concentration in water was investigated by varying the initial concentrations (10, 20, 50, 80 and 100 mg/L) while keeping the dosage at 0.4 g/L constant. Fig 8a shows an increase in the initial phenol concentration from 10 to 100 mg/L resulted in a decrease from 98 to 42 % phenol removal. Similar photocatalytic degradation trends have been reported in literature [58-60]. The possible reason for the deterioration in degradation activity is due to the competitive adsorption of excess phenol molecules to few available active sites at surface of the catalyst. Additionally, it may be possible that the amount of •OH radicals generated reduces with an increase in phenol concentration. As a result, the reaction between the phenolic molecules with the generated electron/hole pairs and hydroxyl radicals

is inhibited. Also, increase in concentration of pollutant results in fewer transmission of photons to the surface as reported in the degradation of Rhodamine B dye using Gelatin/CuS/PVA composite [61].

3.2.4. Effect of pH

Phenol is naturally a very weak acid as it is capable of losing H^+ ions from its OH functional groups [62]. The degradation efficiency is highly dependent on the pH as it affects particle agglomeration, surface properties such as the electrostatic charges and adsorption of pollutant molecules [63]. The zero proton condition (zpc) for ZnO is basic at pH 10, whereas Ag_2S is an ionic and acidic compound, thus the combination is certain to have reduced the number of protons of the overall composite [64]. When dispersed in acidic medium, the surface of the composite tends to be positively charged; likewise, an alkaline solution will result in negatively charged surface. The phenol solution was adjusted by adding in drops, 0.2 M HCl or NaOH to a pH range of 3 to 11 and tested using the Ag/Ag_2S-ZnO catalyst as seen in Fig 8b. At pH 3, only 17 % phenol was removed, this is due to the electrostatic repulsion between the phenol molecules and the very positively charged catalyst surface [62]. In contrast, pH 7 achieved a 97 % degradation since adsorption improved between the negatively charge phenol molecules and positively charged catalyst surface. High pH values of 9 and 11 supports carbonate ions formation, which are scavengers of the OH radicals. As a result, the catalyst surface is negatively charged, phenolate ions dominates the reaction, adsorption becomes weak and degradation efficiency is reduced [65].

3.3. Role of radical species

Photocatalytic degradation is achieved when the hydroxyl and superoxide free radicals and the photo-generated electron/hole pairs attack molecules of the pollutant in aqueous phase [66]. The reactive species (•OH, $O_2•^-$, h^+, and e^-) are likely to reduce and oxidize phenol molecules into lower aliphatic/aromatic compounds and less harmful products [66]. In order to determine the rate-limiting step, scavengers of these photo-induced species were used as diagnostic trappings of the overall photocatalytic degradation process. Fig 8c, revealed a 52 %, 49 %, 6 % and 50 % phenol degradation efficiency upon the addition of IPA, BZQ, TEA and C2N scavengers respectively. IPA, BZQ and C2N exhibited an insignificant influence on photocatalytic activity of Ag/Ag_2S-ZnO compared to TEA, which extremely inhibited the degradation of the pollutant. The dominant quenching effect of the h^+ scavengers can be attributed to the excess movement of electrons to the surface to react with oxygen and the photo-generated superoxide radicals leaving the holes behind. Hence, this investigation has identified $O_2•^-$ as the main active specie of the degradation.

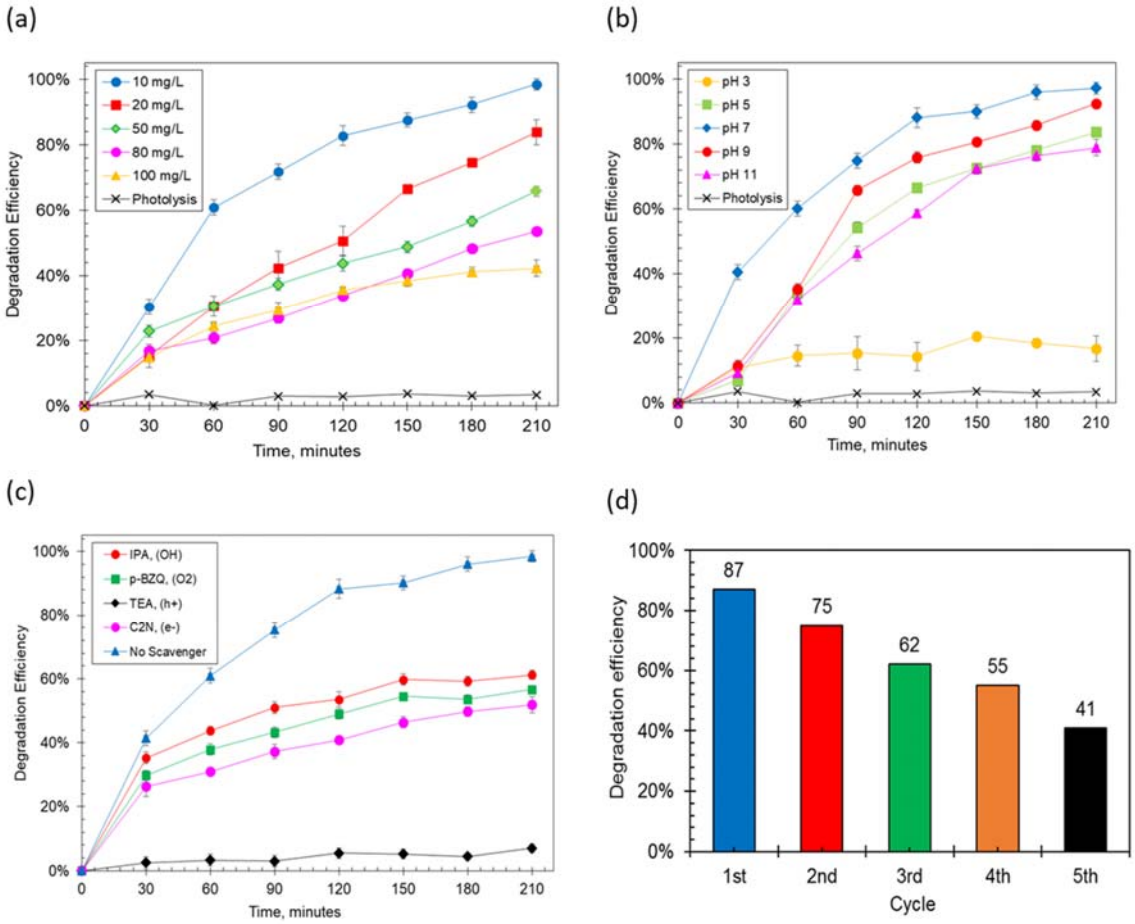

Fig. 8. Effect of (a) initial pollutant concentration and (b) pH using ternary Ag/Ag_2S-ZnO composite; (c) Role of photo-generated radical species degradation test using Ag/Ag_2S-ZnO composite; (d) Ag/Ag_2S-ZnO composite reusability test over five consecutive degradation runs.

3.4. Catalyst recyclability

The ternary Ag/Ag_2S-ZnO catalyst demonstrated good stability in the degradation of phenol after five recycling runs as seen in Fig 8d. After each sequential run, the catalyst particles were recovered by centrifugation followed by decantation before it was re-dispersed into a fresh phenol solution. A gradual relapse of about 12 % in degradation potency was noticed between consecutive cycles. This can be attributed to several reasons such as blocking of surface-active

sites by degradation intermediates/products, which has limited the diffusion of the fresh pollutant molecules through the inner pores to the surface [67, 68]. Reported study on the adsorption of dimethoate onto a Cu-BTC@CA membrane gradually reduced from 321.9 mg/g to 249.4 mg/g resulting in 22.5% loss after 5 recycling runs [15]. In addition, the decline in efficiency may be because of the regression of the catalyst adsorption capacity and/or incomplete photocatalyst regeneration. The amount of substrate accumulated at the surface causes saturation that affects the photonic efficiency of the composite [69]. The first cycle had 87 % phenol degradation and could only degrade 41 % after the fifth cycle.

3.5. Total Organic Carbon (TOC) – Phenol mineralization test

GC/MS analysis of the degradation product identified intermediate peaks with mass/charge (m/z) ratio of 110 (hydroquinone/resorcinol/catechol), 108 (benzoquinone), 118 (succinic acid), and 90 (oxalic acid) (refer to supplementary Fig 1. This is similar to reported results in literature for the photocatalytic degradation of phenol [70]. These intermediate products undergo further mineralization to form ring cleavages of carboxylic acids and aldehydes, which further decarboxylases to give CO_2 and H_2O [71]. TOC mineralization test was conducted using only the ternary Ag/Ag_2S-ZnO catalyst under optimum photocatalytic degradation conditions for 24 hours.

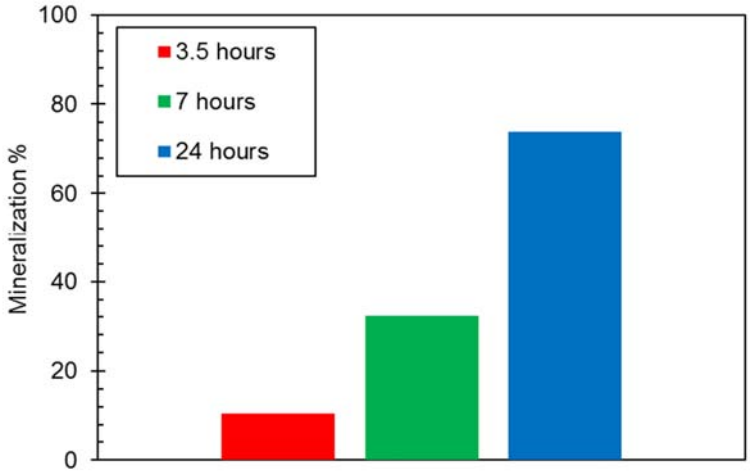

Fig. 9. Total Organic Carbon test for phenol mineralisation

A back-calculation to determine the mass of carbon per litre from the non-purgeable organic carbon (NPOC) of each of the sample, using the carbon mass portion for phenol standard conversion factor (0.766). Fig. 9 showed that the degradation product already had 10 % mineralization in the normal photocatalytic degradation of 3.5 hours. The extent of mineralization, increased to 32 % when the residence time was doubled to 7 hours and further 24 hours resulted in approximately 74 % mineralization. These results affirms that a longer reaction time is needed to achieve a complete mineralization of the phenol intermediates formed after degradation, as they seem to be more obstinate compounds than phenol itself under the same photocatalytic conditions.

3.6. Degradation mechanism

According to the results from the material characterisation and degradation tests conducted, a possible mechanism for the improved photocatalytic degradation was proposed in Fig 10a and b. Semiconductor photocatalyst composites have been successfully synthesised to

narrow the overall bandgap, inhibit e^-/h^+ pair recombination rate, charge separation and enhance photosensitivity in the visible light region. Upon light irradiation (*hv*), the photocatalysts generates electrons and holes (e^-/h^+) pairs at the surface, which are the strong redox agents responsible for efficient degradation. The reaction proceeds as;

$$\text{Photocatalyst composite} + hv \rightarrow \bullet OH + H^+ \quad (5a)$$

Some of the photo-generated e^-/h^+ pairs react with water and oxygen at the surface, as such;

$$O_2 + e^- \rightarrow O_2^{\bullet -} \quad (5b)$$

$$2H_2O + O_2^{\bullet -} + e^- \rightarrow \bullet OH + 2OH^- \quad (5c)$$

$$OH^- + h^+ \rightarrow \bullet OH \quad (5d)$$

In Fig 15a, the conduction and valence bands of ZnO were estimated on the NHE vs eV scale as 0.0 eV and 3.37 eV, and were narrowed with Ag_2S, estimated as -0.007 eV and 1.09 eV. The low bandgap energy of Ag (0.799 eV) generated by photo-deposition further increases the visible light photonic efficiency [72]. These bandgap energies were calculated by the formulas;

$$E_{CB} = X - E_C - 0.5\ E_g \quad (6a)$$

$$E_{VB} = E_{CB} + E_g \quad (6b)$$

Based on the schematic diagram in Fig 15b, metallic Ag_2S had been doped on ZnO to enhance the separation of e^-/h^+ pair such that the electrons are transferred to the metal surface far from the holes. By photo-deposition with visible light activates, the Ag^+ state is photo-reduced to Ag^0 which polarizes the photo-generated e^-/h^+ by SPR effect. The plasmonic effect of Ag^0 on the composite causes the electron to be farther away from the interface with holes at the Ag_2S-ZnO surface [73]. Phenol degradation was facilitated by strong oxidizing agents such

that; at the surface, electrons oxidizes oxygen to form superoxide radicals ($O^{\bullet -}_2$) while the holes oxidizes the S and Zn to SO^{2-}_4 and Zn^{2+} ions in their reduced form respectively [74]. In reference to the degradation radical forensic test conducted as shown in Fig 8c, the addition of the triethanolamine (h^+ scavenger) drastically inhibited the reaction process; suggesting that the photo-generated holes are the primary drivers for the degradation mechanism. Generally, the mechanism postulates that while ZnO provides the surface area, photo-deposition of Ag/Ag_2S increase the actives sites, as the Ag^+ tends to contribute to the overall composite chemical stability [75].

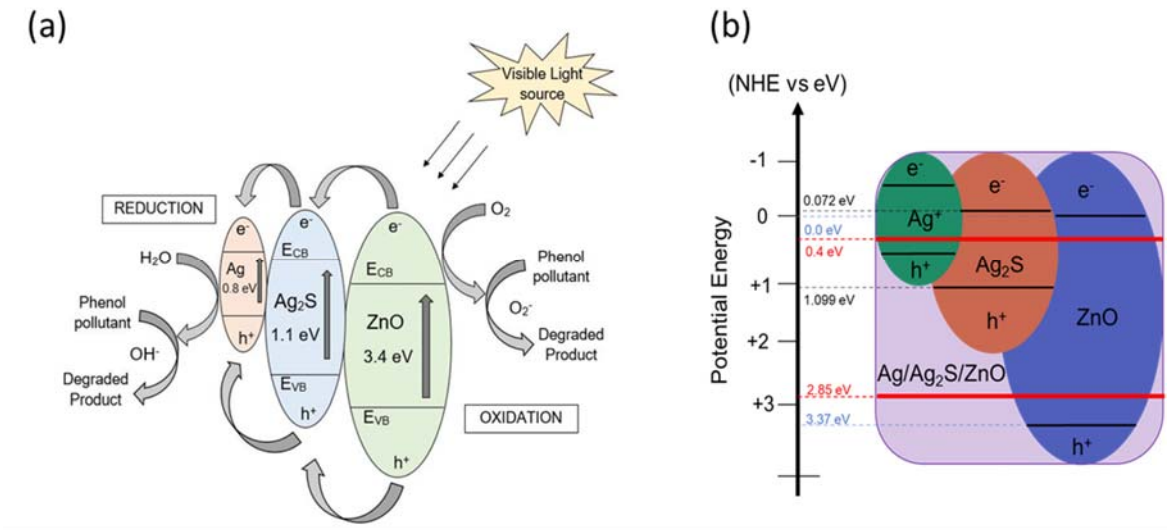

Fig. 10. (a) Mechanism of Ag/Ag2S-ZnO photocatalysis and (b) Schematic NHE vs eV bandgap tailoring.

4. Conclusions

An SPR-enhanced composite based on Ag/Ag_2S and ZnO for visible light responsiveness were prepared by a simple hydrothermal method followed by photo-deposition. The composites were characterised using various techniques to ascertain their crystallinity, purity,

morphology, absorption potential and chemical states. Degradation parameters such as catalyst dosage, initial concentration, effect of pH were optimized using the target composite, Ag/Ag_2S-ZnO. The as-synthesised composites demonstrated excellent photocatalytic activity at 0.4 g/L loading for the degradation of 10 mg/L phenol in water under 3.5 hours of visible light illumination. Investigations on the effect of light intensity under simulated and real solar (sun) visible light is recommended. The role of the photo-induced radical species was elucidated through scavenging tests, the holes and superoxide radicals were identified as the main species for photodegradation. Phenol achieved 74 % mineralization to CO_2 and H_2O after 24 hours residence time. The recycling test revealed a gradual 12 % loss in activity after consecutive runs, therefore future work on the recovery method and regeneration of the catalyst is recommended. This work reports a novel way to develop highly enhanced visible-light-induced photocatalyst composites, which could be applied in the development of hybrid materials for polluted water treatment.

CRediT authorship contribution statement

Emmanuel O. Ichipi: Methodology, Formal analysis, Investigation, Visualisation, Data curation, Roles/writing - original draft, Writing – review and editing, Project administration. **Shepherd M. Tichapondwa:** Validation, Formal analysis, Supervision, Writing – review and editing Conceptualisation, Data curation, and Supervision. **Evans M. N. Chirwa:** Funding acquisition, Conceptualisation, Resources, Supervision, Validation, Writing – review and editing

Declaration of Competing Interest

The authors declare that they have no known competing financial interests or personal relationships with other people or organisations that could have appeared to influence the work reported in this paper.

Acknowledgements

This work was supported by the National Research Foundation of South Africa (Grant numbers: CSUR180215313534, TTK18024324064) and Sedibeng Water Chair awarded to Prof Evans MN Chirwa and Dr Shepherd SM Tichapondwa. The authors would like to acknowledge the support from the Water Utilisation division, Department of Chemical Engineering (University of Pretoria).

List of Nomeclature

Ag	Silver
Ag_2S	Silver sulphide
BET	Brunauer-Emmett-Teller
C2N	Cupper (II) nitrate
C_B	Conduction band
e^-/h^+	electron/hole
eV	electron Volt
FTIR	Fourier-Transform Infrared
g/L	gram per Litre

HPLC	High Performance liquid Chromatography
IPA	Isopropyl alcohol
K_{max}	maximum rate constant
min	minutes
mg/L	milligram per Litre
mL	millilitres
nm	nanometre
p-BZQ	p-Benzoquinone
PL	Photoluminescence
SEM	Scanning electron microscope
SPR	Surface Plasmon Resonance
TEA	Triethanolamine
TEM	Transmission electron microscope
UV	Ultraviolet
UV-Vis	Ultraviolet-Visible
V_B	Valence band
XPS	X-ray Photoelectron Spectroscopy
XRD	X-ray Diffraction
ZnO	Zinc Oxide

References

[1] E. M. Cuerda-Correa, M. F. Alexandre-Franco, and C. Fernández-González, "Advanced Oxidation Processes for the Removal of Antibiotics from Water. An Overview," *Water,* vol. 12, no. 1, (2020), p. 102. doi: doi:10.3390/w12010102

[2] C. Belver, J. Bedia, A. Gómez-Avilés, M. Peñas-Garzón, and J. J. Rodriguez, "Chapter 22 - Semiconductor Photocatalysis for Water Purification," in *Nanoscale Materials in Water Purification*, S. Thomas, D. Pasquini, S.-Y. Leu, and D. A. Gopakumar, Eds.: Elsevier, 2019, pp. 581-651.

[3] E. Bamuza-Pemu and E. Chirwa, "Photocatalytic degradation of geosmin: Reaction pathway analysis," *Water SA,* vol. 38, (2012), p. 689. doi: 10.4314/wsa.v38i5.6

[4] K. Ozawa, M. Emori, S. Yamamoto, R. Yukawa, S. Yamamoto, R. Hobara, K. Fujikawa, H. Sakama, and I. Matsuda, "Electron–Hole Recombination Time at TiO2 Single-Crystal Surfaces: Influence of Surface Band Bending," *The Journal of Physical Chemistry Letters,* vol. 5, (2014), pp. 1953–1957. doi: 10.1021/jz500770c

[5] V. Binas, D. Venieri, D. Kotzias, and G. Kiriakidis, "Modified TiO2 based photocatalysts for improved air and health quality," *Journal of Materiomics,* vol. 3, no. 1, (2017), pp. 3-16. doi: https://doi.org/10.1016/j.jmat.2016.11.002

[6] V. Etacheri, C. Di Valentin, J. Schneider, D. Bahnemann, and S. C. Pillai, "Visible-light activation of TiO2 photocatalysts: Advances in theory and experiments," *Journal of Photochemistry and Photobiology C: Photochemistry Reviews,* vol. 25, (2015), pp. 1-29. doi: https://doi.org/10.1016/j.jphotochemrev.2015.08.003

[7] R. Nakano, R. Chand, E. Obuchi, K. Katoh, and K. Nakano, "Performance of TiO2 photocatalyst supported on silica beads for purification of wastewater after absorption of reflow exhaust gas," *Chemical engineering journal,* vol. 176, (2011), pp. 260-264.

[8] N. Moloto, S. Mpelane, L. M. Sikhwivhilu, and S. Sinha Ray, "Optical and Morphological Properties of ZnO- and TiO₂-Derived Nanostructures Synthesized via a Microwave-Assisted Hydrothermal Method," *International Journal of Photoenergy,* vol. 2012, (2012), p. 189069. doi: 10.1155/2012/189069

[9] P. Fageria, S. Gangopadhyay, and S. Pande, "Synthesis of ZnO/Au and ZnO/Ag nanoparticles and their photocatalytic application using UV and visible light," *RSC Advances,* 10.1039/C4RA03158J vol. 4, no. 48, (2014), pp. 24962-24972. doi: 10.1039/C4RA03158J

[10] F. Zhang, X. Wang, H. Liu, C. Liu, Y. Wan, Y. Long, and Z. Cai, "Recent Advances and Applications of Semiconductor Photocatalytic Technology," *Applied Sciences,* vol. 9, (2019), p. 2489. doi: 10.3390/app9122489

[11] X. Li, S. Fang, L. Ge, C. Han, P. Qiu, and W. Liu, "Synthesis of flower-like Ag/AgCl-Bi2MoO6 plasmonic photocatalysts with enhanced visible-light photocatalytic performance," *Applied Catalysis B: Environmental,* vol. 176-177, (2015), pp. 62-69. doi: https://doi.org/10.1016/j.apcatb.2015.03.042

[12] Q. Yuhuan, H. Mingming, and L. Zhaohui, "Metal–organic frameworks for photocatalysis,"*Interface Science and Technology,* vol. 31, (2020), pp. 541-579. doi: https://doi.org/10.1016/B978-0-08-102890-2.00017-8

[13] N. Wei, K. Anish, "Chapter 10 - Modified metal-organic frameworks as photocatalysts," *Metal-Organic Frameworks for Chemical Reactions,* vol. 81, (2021), pp. 231-270. ISBN 9780128220993 doi: https://doi.org/10.1016/B978-0-12-822099-3.00010-1

[14] A. Younis, E. Kwon, Q. Muhammad, K. Ki-Hyun, K. Taejin, K.Deepak, D. Xiaomin, and A. Imran, "Metal-organic framework as a photocatalyst: Progress in modulation strategies and environmental/energy applications,"*Progress in Energy and Combustion Science,* vol. 81, (2020), pp. 100870. ISSN 0360-1285 doi: https://doi.org/10.1016/j.pecs.2020.100870

[15] M. Abdelhameed, H. Abdel-Gawad, and E. Emam, "Macroporous Cu-MOF@cellulose acetate membrane serviceable in selective removal of dimethoate pesticide from wastewater," *Journal of Environmental Chemical Engineering,* vol. 9, (2021), 105121 doi: https://doi.org/10.1016/j.jece.2021.105121

[16] E. Emam, B. Ahmed, E. Gomaa, H. Helal, M. Abdelhameed, "Recyclable photocatalyst composites based on Ag3VO4 and Ag2WO4 @MOF@cotton for effective discoloration of dye in visible light," *Cellulose,* vol. 27, (2020), pp. 7139–7155. doi: https://doi.org/10.1007/s10570-020-03282-8

[17] M. Abdelhameed, M. El-Shahat, and E. Emam, "Employable Metal (Ag & Pd)@MIL-125-NH2@Cellulose Acetate Film For Visible-light Driven Photocatalysis For Reduction of Nitro-aromatics," *Carbohydrate Polymers,* vol. 247, (2020), pp. 116695. doi: https://doi.org/10.1016/j.carbpol.2020.116695

[18] P. Singh, R. Kumar, and R. Singh, "Progress on Transition Metal-Doped ZnO Nanoparticles and Its Application," *Industrial & Engineering Chemistry Research,* vol. 58, (2019). doi: 10.1021/acs.iecr.9b01561

[19] M. D. Tyona, R. U. Osuji, P. U. Asogwa, S. B. Jambure, and F. I. Ezema, "Structural modification and band gap tailoring of zinc oxide thin films using copper impurities," *Journal of Solid State Electrochemistry,* vol. 21, no. 9, (2017), pp. 2629-2638. doi: 10.1007/s10008-017-3533-3

[20] P. Singh, R. Kumar, and R. K. Singh, "Progress on Transition Metal-Doped ZnO Nanoparticles and Its Application," *Industrial & Engineering Chemistry Research,* vol. 58, no. 37, (2019), pp. 17130-17163. doi: 10.1021/acs.iecr.9b01561

[21] Q. Jiang, C. Ji, D. J. Riley, and F. Xie, "Boosting the Efficiency of Photoelectrolysis by the Addition of Non-Noble Plasmonic Metals: Al & Cu," *Nanomaterials,* vol. 9, no. 1, (2019). doi: 10.3390/nano9010001

[22] Z. Jiao, J. Zhang, Z. Liu, and Z. Ma, "Ag/AgCl/Ag2MoO4 composites for visible-light-driven photocatalysis," *Journal of Photochemistry and Photobiology A: Chemistry,* vol. 371, (2019), pp. 67-75. doi: https://doi.org/10.1016/j.jphotochem.2018.11.003

[23] P. Wang, B. Huang, X. Zhang, X. Qin, H. Jin, Y. Dai, Z. Wang, J. Wei, J. Zhan, S. Wang, J. Wang, and M.-H. Whangbo, "Highly Efficient Visible-Light Plasmonic

Photocatalyst Ag@AgBr," *Chemistry – A European Journal,* vol. 15, no. 8, (2009), pp. 1821-1824. doi: https://doi.org/10.1002/chem.200802327

[24] A. K. Pal and D. B. Mohan, "The Study of Surface Plasmon Enhanced Emission of ZnO Nanorods on Plasmonic Ag Nanorods Array," *Materials Today: Proceedings,* vol. 2, no. 9, Part A, (2015), pp. 4407-4412. doi: https://doi.org/10.1016/j.matpr.2015.10.040

[25] J. You, X. Zhang, Y. Fan, Z. Yin, P. Cai, and N. Chen, "Effects of the morphology of ZnO/Ag interface on the surface-plasmon-enhanced emission of ZnO films," *Journal of Physics D,* vol. 41, (2008), p. 205101.

[26] C. W. Cheng, E. J. Sie, B. Liu, C. H. A. Huan, T. C. Sum, H. D. Sun, and H. J. Fan, "Surface plasmon enhanced band edge luminescence of ZnO nanorods by capping Au nanoparticles," *Applied Physics Letters,* vol. 96, no. 7, (2010), p. 071107. doi: 10.1063/1.3323091

[27] J. Li, B. Liu, A. Wu, B. Yang, W. Yang, F. Liu, X. Zhang, V. An, and X. Jiang, "Composition and Band Gap Tailoring of Crystalline (GaN)1–x(ZnO)x Solid Solution Nanowires for Enhanced Photoelectrochemical Performance," *Inorganic Chemistry,* vol. 57, no. 9, (2018), pp. 5240-5248. doi: 10.1021/acs.inorgchem.8b00277

[28] Y. Ao, H. Tang, P. Wang, and C. Wang, "Deposition of Ag@AgCl onto two dimensional square-like BiOCl nanoplates for high visible-light photocatalytic activity," *Materials Letters,* vol. 131, (2014), pp. 74-77. doi: https://doi.org/10.1016/j.matlet.2014.05.083

[29] M. A. Borysiewicz, "ZnO as a Functional Material, a Review," *Crystals,* vol. 9, no. 10, (2019). doi: 10.3390/cryst9100505

[30] H. Granbohm, J. Larismaa, S. Ali, L.-S. Johansson, and S.-P. Hannula, "Control of the Size of Silver Nanoparticles and Release of Silver in Heat Treated SiO_2-Ag Composite Powders," *Materials (Basel, Switzerland),* vol. 11, (2018). doi: 10.3390/ma11010080

[31] X. Wang, J. Liu, S. Leong, X. Lin, J. Wei, B. Kong, Y. Xu, Z.-X. N. Low, J. Yao, and H.-T. Wang, "Rapid Construction of ZnO@ZIF-8 Heterostructures with Size-Selective Photocatalysis Properties," *ACS applied materials & interfaces,* vol. 8, (2016). doi: 10.1021/acsami.6b00028

[32] J. Gamage McEvoy, W. Cui, and Z. Zhang, "Synthesis and characterization of Ag/AgCl–activated carbon composites for enhanced visible light photocatalysis," *Applied Catalysis B: Environmental,* vol. 144, (2014), pp. 702-712. doi: https://doi.org/10.1016/j.apcatb.2013.07.062

[33] H. Zhang, X. Fan, X. Quan, S. Chen, and H. Yu, "Graphene Sheets Grafted Ag@AgCl Hybrid with Enhanced Plasmonic Photocatalytic Activity under Visible Light," *Environmental Science & Technology,* vol. 45, no. 13, (2011), pp. 5731-5736. doi: 10.1021/es2002919

[34] S. Sadovnikov and A. Gusev, "Effect of Particle Size and Specific Surface Area on the Determination of the Density of Nanocrystalline Silver Sulfide Ag2S Powders," *Physics of the Solid State,* vol. 60, (2018), pp. 877-881. doi: 10.1134/S106378341805027X

[35] J. Rouquerol, D. Avnir, C. W. Fairbridge, D. H. Everett, J. M. Haynes, N. Pernicone, J. D. F. Ramsay, K. S. W. Sing, and K. K. Unger, "Recommendations for the characterization of porous solids (Technical Report)," *Pure and Applied Chemistry,* vol. 66, no. 8, (1994), pp. 1739-1758. doi: doi:10.1351/pac199466081739

[36] M. Thommes and K. Cychosz, "Physical adsorption characterization of nanoporous materials: Progress and challenges," *Adsorption,* vol. 20, (2014). doi: 10.1007/s10450-014-9606-z

[37] K. Handore, S. Bhavsar, A. Horne, P. Chhattise, K. Mohite, J. Ambekar, N. Pande, and V. Chabukswar, "Novel Green Route of Synthesis of ZnO Nanoparticles by Using Natural Biodegradable Polymer and Its Application as a Catalyst for Oxidation of Aldehydes," *Journal of Macromolecular Science Part A*

Pure and Applied Chemistry, vol. 51, (2014), p. 941. doi: 10.1080/10601325.2014.967078

[38] M. Pudukudy and Z. Yaakob, "Facile Synthesis of Quasi Spherical ZnO Nanoparticles with Excellent Photo catalytic Activity," *Journal of Cluster Science,* vol. 26, (2014). doi: 10.1007/s10876-014-0806-1

[39] W. Yang, L. Wang, X. Lu, Y. Ding, and Q. Zhang, "The effect of concentration precursor reagents on the excitation spectra of the ZnO quantum dots in the solution," *Materials Letters,* vol. 141, (2015), pp. 330-332. doi: https://doi.org/10.1016/j.matlet.2014.11.117

[40] W. Yang, B. Zhang, Q. Zhang, L. Wang, B. Song, Y. Ding, and C. P. Wong, "Adjusting the band structure and defects of ZnO quantum dots via tin doping," *RSC Advances,* 10.1039/C6RA25940E vol. 7, no. 19, (2017), pp. 11345-11354. doi: 10.1039/C6RA25940E

[41] D. Raoufi, "Synthesis and photoluminescence characterization of ZnO nanoparticles," *Journal of Luminescence,* vol. 134, (2013), pp. 213-219. doi: 10.1016/j.jlumin.2012.08.045

[52] R. Khokhra, B. Bharti, H.-N. Lee, and R. Kumar, "Visible and UV photo-detection in ZnO nanostructured thin films via simple tuning of solution method," *Scientific Reports,* vol. 7, (2017). doi: 10.1038/s41598-017-15125-x

[43] L. Saikia, D. Bhuyan, M. Saikia, B. Malakar, D. Dutta, and P. Sengupta, "Photocatalytic performance of ZnO nanomaterials for self sensitized degradation of Malachite Green dye under solar light," *Applied Catalysis A: General,* vol. 490, (2014). doi: 10.1016/j.apcata.2014.10.053

[44] J. Jiang and L. Zhang, "Rapid Microwave-Assisted Nonaqueous Synthesis and Growth Mechanism of AgCl/Ag, and Its Daylight-Driven Plasmonic Photocatalysis," *Chemistry – A European Journal,* vol. 17, no. 13, (2011), pp. 3710-3717. doi: https://doi.org/10.1002/chem.201002951

[45] P. Wang, B. Huang, Z. Lou, X. Zhang, X. Qin, Y. Dai, Z. Zheng, and X. Wang, "Synthesis of Highly Efficient Ag@AgCl Plasmonic Photocatalysts with Various

Structures," *Chemistry – A European Journal,* vol. 16, no. 2, (2010), pp. 538-544. doi: https://doi.org/10.1002/chem.200901954

[46] H.C. Tseng and Y.W. Chen, "Facile Synthesis of Ag/TiO2 by Photoreduction Method and Its Degradation Activity of Methylene Blue under UV and Visible Light Irradiation," *Modern Research in Catalysis,* vol. 9, no. 01, (2019), doi: https://doi.org/10.4236/mrc.2020.91001

[47] N. Mirikaram, Á. Pérez-Molina, . S. Morales-Torres, A. Salemi, F. J. Maldonado-Hódar and L. M. Pastrana-Martínez, "Photocatalytic Perfomance of ZnO-Graphene Oxide Composites towards the Degradation of Vanillic Acid under Solar Radiation and Visible-LED," Nanomaterials (Basel), vol. 6, no. 15, 2021. doi: https://doi.org/10.3390/nano11061576

[48] A.H. Khavar, G. Moussavi, A.R. Mahjoub, R. Luque, D. Rodríguez-Padrón, and M. Sattari, "Enhanced visible light photocatalytic degradation of acetaminophen with Ag2S-ZnO@rGO core-shell microsphere as a novel catalyst: Catalyst preparation and characterization and mechanistic catalytic experiments", *Separation and Purification Technology,* vol. 229, (2019), 115803. doi: https://doi.org/10.1016/j.seppur.2019.115803

[49] S. Khanchandani, P.K. Srivastava, S. Kumar, S. Ghosh, and A.K. Ganguli, "Band Gap Engineering of ZnO using Core/Shell Morphology with Environmentally Benign Ag2S Sensitizer for Efficient Light Harvesting and Enhanced Visible-Light Photocatalysis", *Inorganic Chemistry,* vol. 53, (2014), pp. 8902-8912. doi: https://doi.org/10.1021/ic500518a

[50] A. Ziashahabi, M. Prato, Z. Dang, R. Poursalehi, and N. Naseri, "The effect of silver oxidation on the photocatalytic activity of Ag/ZnO hybrid plasmonic/metal-oxide nanostructures under visible light and in the dark" , *Scientific Reports,* vol. 9, (2019), 11839. doi: https://doi.org/10.1038/s41598-019-48075-7

[51] Q. Cao, R. Che, and N. Chen, "Facile and rapid growth of Ag2S microrod arrays as efficient substrates for both SERS detection and photocatalytic degradation

of organic dyes", *Chemical Communications,* vol. 50, (2014), pp. 4931-4933. doi: https://doi.org/10.1039/C4CC00107A

[52] S. Shuang, R. LV, X. Cui, Z. Xie, J. Zheng, and Z. Zhang, "Efficient photocatalysis with graphene oxide/Ag/Ag2S–TiO2 nanocomposites under visible light irradiation", *RSC Advances,* vol. 8, (2018), pp. 5784-5791. doi: https://doi.org/10.1039/C7RA13501G

[53] P. Huo, C. Liu, D. Wu, J. Guan, J. Li, H. Wang, Q. Tang, X. Li, Y. Yan, and S. Yuan, "Fabricated Ag/Ag 2 S/reduced graphene oxide composite photocatalysts for enhancing visible light photocatalytic and antibacterial activity", *Journal of Industrial and Engineering Chemistry,* vol. 57, (2017), doi: https://doi.org/10.1016/j.jiec.2017.08.015

[54] S. Li, C. Wang, Y. Liu, B. Xue, W. Jiang, Y. Liu, L. Mo, and X. Chen, "Photocatalytic degradation of antibiotics using a novel Ag/Ag2S/Bi2MoO6 plasmonic p-n heterojunction photocatalyst: Mineralization activity, degradation pathways and boosted charge separation mechanism", *Chemical Engineering Journal,* vol. 415, (2021), 128991. doi: https://doi.org/10.1016/j.cej.2021.128991

[55] F. Aisien, A. Amenaghawon, and E. Ekpenisi, "Photocatalytic decolourisation of industrial wastewater from a soft drink company," *Journal of Engineering and Applied Sciences,* vol. 9, (2014), pp. 11-16. SSN: 1119-8109.

[56] V. Kumar, K. Porkodi, and F. Rocha, "Langmuir Hinshelwood Kinetics – a Theoretical Study," *Catalysis Communications - CATAL COMMUN,* vol. 9, (2008), pp. 82-84. doi: 10.1016/j.catcom.2007.05.019

[57] J. Matos, J. Laine, and J. M. Herrmann, "Effect of the Type of Activated Carbons on the Photocatalytic Degradation of Aqueous Organic Pollutants by UV-Irradiated Titania," *Journal of Catalysis,* vol. 200, no. 1, (2001), pp. 10-20. doi: https://doi.org/10.1006/jcat.2001.3191

[58] M. F. Hanafi and N. Sapawe, "Effect of initial concentration on the photocatalytic degradation of remazol brilliant blue dye using nickel catalyst,"

Materials Today: Proceedings, vol. 31, (2020), pp. 318-320. doi: https://doi.org/10.1016/j.matpr.2020.06.066

[59] K. M. Reza, A. S. W. Kurny, and F. Gulshan, "Parameters affecting the photocatalytic degradation of dyes using TiO2: a review," *Applied Water Science,* vol. 7, no. 4, (2017), pp. 1569-1578. doi: 10.1007/s13201-015-0367-y

[60] D. Zhang, S. Lv, and Z. Luo, "A study on the photocatalytic degradation performance of a [KNbO3]0.9-[BaNi0.5Nb0.5O3−δ]0.1 perovskite," *RSC Advances,* 10.1039/C9RA07310H vol. 10, no. 3, (2020), pp. 1275-1280. doi: 10.1039/C9RA07310H

[61] A. Al Kahtani, "Photocatalytic Degradation of Rhodamine B Dye in Wastewater Using Gelatin/CuS/PVA Nanocomposites under Solar Light Irradiation," *Journal of Biomaterials and Nanobiotechnology,* vol. 08, (2017), pp. 66-82. doi: 10.4236/jbnb.2017.81005

[62] W. Vermerris and R. Nicholson, *Phenolic compound biochemistry*. Springer Science & Business Media, 2007.

[63] A. Alkaim, A. Aljeboree, N. A. Alrazaq, S. Jaafer, F. Hussein, and A. J. Lilo, "Effect of pH on Adsorption and Photocatalytic Degradation Efficiency of Different Catalysts on Removal of Methylene Blue," *Asian Journal of Chemistry,* vol. 26, (2014), pp. 8445-8448. doi: 10.14233/ajchem.2014.17908

[64] S. S. Alias, A. B. Ismail, and A. A. Mohamad, "Effect of pH on ZnO nanoparticle properties synthesized by sol–gel centrifugation," *Journal of Alloys and Compounds,* vol. 499, no. 2, (2010), pp. 231-237. doi: https://doi.org/10.1016/j.jallcom.2010.03.174

[65] F. Akbal and N. Onar, "Photocatalytic Degradation of Phenol," *Environmental monitoring and assessment,* vol. 83, (2003), pp. 295-302. doi: 10.1023/A:1022666322436

[66] D. Chatterjee and S. Dasgupta, "Visible light induced photocatalytic degradation of organic pollutants," *Journal of Photochemistry and*

Photobiology C: Photochemistry Reviews, vol. 6, no. 2, (2005), pp. 186-205. doi: https://doi.org/10.1016/j.jphotochemrev.2005.09.001

[67] Y. Ao, J. Xu, D. Fu, X. Shen, and C. Yuan, "Low temperature preparation of anatase TiO2-coated activated carbon," *Colloids and Surfaces A: Physicochemical and Engineering Aspects,* vol. 312, no. 2, (2008), pp. 125-130. doi: https://doi.org/10.1016/j.colsurfa.2007.06.039

[68] S. X. Liu, X. Y. Chen, and X. Chen, "A TiO2/AC composite photocatalyst with high activity and easy separation prepared by a hydrothermal method," *Journal of Hazardous Materials,* vol. 143, no. 1, (2007), pp. 257-263. doi: https://doi.org/10.1016/j.jhazmat.2006.09.026

[69] J. Araña, J. L. Martínez Nieto, J. A. Herrera Melián, J. M. Doña Rodríguez, O. González Díaz, J. Pérez Peña, O. Bergasa, C. Alvarez, and J. Méndez, "Photocatalytic degradation of formaldehyde containing wastewater from veterinarian laboratories," *Chemosphere,* vol. 55, no. 6, (2004), pp. 893-904. doi: https://doi.org/10.1016/j.chemosphere.2003.11.060

[70] L. Andrade, L. A, O. de, R.-F. C, and C. B, "Development of a HPLC method to follow the degradation of phenol by electrochemical or photoelectrochemical treatment," *Journal of the Brazilian Chemical Society,* vol. 17, (2006). doi: 10.1590/S0103-50532006000200022

[71] D. Suryaman, K. Hasegawa, and S. Kagaya, "Combined biological and photocatalytic treatment for the mineralization of phenol in water," *Chemosphere,* vol. 65, no. 11, (2006), pp. 2502-2506. doi: https://doi.org/10.1016/j.chemosphere.2006.07.059

[72] S. Bhardwaj, D. Sharma, P. Kumari, and B. Pal, "Influence of photodeposition time and loading amount of Ag co-catalyst on growth, distribution and photocatalytic properties of Ag@TiO2 nanocatalysts," *Optical Materials,* vol. 106, (2020), p. 109975. doi: https://doi.org/10.1016/j.optmat.2020.109975

[73] P. Wang, B. Huang, X. Qin, X. Zhang, Y. Dai, J. Wei, and M.-H. Whangbo, "Ag@AgCl: A Highly Efficient and Stable Photocatalyst Active under Visible

Light," *Angewandte Chemie International Edition,* vol. 47, no. 41, (2008), pp. 7931-7933. doi: https://doi.org/10.1002/anie.200802483

[74] J. Yu, G. Dai, and B. Huang, "Fabrication and Characterization of Visible-Light-Driven Plasmonic Photocatalyst Ag/AgCl/TiO2 Nanotube Arrays," *The Journal of Physical Chemistry C,* vol. 113, no. 37, (2009), pp. 16394-16401. doi: 10.1021/jp905247j

[75] B. Díez-Buitrago, J. Barroso, L. Saa, N. Briz, and V. Pavlov, "Facile Synthesis and Characterization of Ag/Ag2S Nanoparticles Enzymatically Grown In Situ and their Application to the Colorimetric Detection of Glucose Oxidase," *ChemistrySelect,* vol. 4, no. 28, (2019), pp. 8212-8219. doi: https://doi.org/10.1002/slct.201901673